A Computational and Experimental Study on the Binding of Dithio Ligands to Sperrylite, Pentlandite, and Platinum

A Computational and Experimental Study on the Binding of Dithio Ligands to Sperrylite, Pentlandite and Platinum. Calum N. Waterson,[a] Peter A. Tasker,[a] Raymond Farinato,[b] D. R. Nagaraj,[b] Natalie Shackleton,[c] and Carole A. Morrison[a,*]

[a]School of Chemistry and EaSTCHEM Research School, University of Edinburgh, The King's Buildings, David Brewster Road, Edinburgh EH9 3FJ, UK.

[b]Cytec Solvay Group, 1937 West Main St, Stamford, CT, 06902, USA

[c]Anglo American Technical Solutions, 8 Schonland St, Theta Johannesburg, PO Box 106, Crown Mines 2025, South Africa.

c.morrison@ed.ac.uk

Abstract

This benchmark study documents a combined computational and experimental investigation into the binding of three commercial dithio collector ligands used in industrial froth flotation processes to separate high value minerals from lower value material. First principles condensed matter simulations showed that ethyl xanthate, N,N-diethyl dithiocarbamate and diisobutyl dithiophospinate anions all bind least strongly to the [100] Miller index plane of the platinum-containing mineral sperrylite, followed by the [111] MI surface of the mixed nickel/iron sulphide mineral pentlandite, while all ligands showed strongest binding affinity to the [111] MI surface model of pure platinum. Calculations also support experimental observations that neutral ethyl xanthogen disulphide formed on oxidation of ethyl xanthate binds much more weakly than the monomer. A monolayer of water molecules would easily be displaced from all surfaces by any of the collector ligands. The hydroxide anion was found to have binding energies of comparable magnitude to the collector ligands on all surfaces. Cyclic voltammetry measurements performed on working electrodes constructed from sperrylite, pentlandite and platinum permitted measurement of the mixed oxidation potential associated with the surface dimerization reaction for all three collector ligands, although the data obtained for diisobutyl dithiophospinate was less clear cut than for the other ligands. Comparison of the relative ordering of the mixed potentials for the three ligands gave a favourable match with the predicted outcome of binding energy strengths obtained from the modelling study. This study demonstrates that first principles simulations can be used to predict the binding energies of collector ligands to mineral and metallic surfaces.

1.0 Introduction

The mining, recovery and processing of platinum group elements from their ores is a multi-billion dollar industry. One of the biggest challenges associated with this industry is separating the relatively low-abundance platinum group minerals from the vast excess of commercially worthless rock which is also extracted during mining. The most widely applied separation process employed is froth flotation,[1] a physicochemical method which separates mixtures of solids on the basis of their relative hydrophobicities. The flotation process operates by dispersing finely-ground solids into agitated water tanks through which air is passed. This presents a gas-liquid interface onto which the more hydrophobic particles can attach. The subsequent rising of the particle-laden bubbles leads to a froth at the surface of the tank, which is mechanically separated for further processing.

Control of the chemistry occurring within the flotation process can allow enhanced recovery of a particular mineral over others. This is achieved by the addition of collector ligands, which are small organic molecules that adsorb preferentially on the surfaces of target minerals and modulate their surface hydrophobicity by

presenting a short-chain aliphatic tail into solution, which in turn promotes mineral/bubble attachment and improves recovery. Understanding the mode of action by which collector ligands interact with mineral surfaces may therefore lead to improvements in ligand design and subsequent improvements in mineral recovery.

For almost a century, the xanthate family of collector molecules (a subclass of dithio collectors which conform to the general formula $R\text{-}OCS_2^-$, where R is a short linear or branched chain saturated hydrocarbon) has been the industrial workhorse of the mineral processing industry.[2] The adsorption of ethyl xanthate (EX) at metal and mineral surfaces can be studied electrochemically by taking advantage of its redox behaviour. Of particular note is the early voltammetry work by Woods[3] on the additive, oxidative dimerisation reaction of adsorbed xanthates on surfaces such as Pt and Au, which is balanced by a corresponding reduction of molecular oxygen, as outlined in equations (1)-(3). Neglecting mass transfer effects, the rate of these reactions is largely dependent upon the cell potential in relation to the equilibrium potential of the $EX/(EX)_2$ redox reaction and the stability of the adsorbed species $(EX)_{ads}$.

$$EX^- \rightarrow (EX)_{ads} + e^- \quad (1)$$

$$(EX)_{ads} + EX^- \rightarrow (EX)_{2,ads} + e^- \quad (2)$$

$$½\ O_2 + H_2O + 2e^- \rightarrow 2OH^- \quad (3)$$

Since the publication of Woods' paper a number of others ,[4-5] notably by Vermaak and co-workers,[6-8] also reported contact angle measurements to study the formation of air/nitrogen bubbles directly on the surface of xanthate-bound minerals (including $PtAs_2$,[6] $Pt\text{-}Te_2$,[7] Pt-Bi-Te,[7] and Pd-Bi-Te[8]) under electrochemically-induced oxidising conditions. Their data displays a clear correlation between the dimerization of the xanthate collector ligands and contact angle, with the mineral surfaces displaying poor hydrophobicity at potentials below that required for dimerization, and increasing hydrophobicity above. These reports strongly suggest that for these mineral surfaces formation of $(EX)_2$ is the principal cause of the increase in surface hydrophobicity, and hence the improved mineral recovery in the presence of the collector ligand. Raman and Surface enhanced Raman spectroscopy (SERS) measurements also confirmed that xanthate monomers chemisorb to metal and mineral surfaces, and found evidence for the formation of metal complexes on surfaces. The appearance of dixanthogen at higher oxidation potentials through the appearance of the S-S stretching mode was also reported.[6-13] The surface enhancement effect for dixanthogen bound to a gold surface was very weak, however, which led Woods *et al.*[9] to propose that dixanthogen species were more likely to form physisorbed multilayers above the chemisorbed monomer. Other work by Mermillod-Blondin *et al.*[10] for xanthate on pyrite (FeS_2) cites a combination of metal-xanthate species overlaid by multilayers of $(EX)_2$ as being the species involved in inducing flotation, which tallies with the general findings of both Woods and Vermaak. However, for other metal and mineral surfaces, and for other collector ligands, the nature of the surface interactions is still a matter of some debate.[13-15]

Gaining an atomistic level of detail for the adsorption of collector ligands presented to mineral surfaces can also be approached through a computational modelling study. To obtain high accuracy results for a mixed organic/inorganic system requires a first-principles condensed matter approach, with plane-wave density functional theory (DFT) presenting the most tractable solution.[16] Modelling such complex systems is not without its own challenges, however, and the opportunity to be able to benchmark the results obtained from simulation against an experimental study is extremely desirable. Assuming that the collector ligand binds to the surface, and that the ligand adsorption/dimerization reactions shown in equations (1)-(3) involve reorganisation of the adsorbed xanthate-metal species which will sever some metal-ligand bonds to

permit formation of a disulphide bond, [3, 15] this then raises the question as to whether electrochemical measurements using working electrodes made from the minerals may be utilised to validate the ligand/surface binding energies obtained from computational modelling.

In this paper, we first present the results obtained in the computational ligand binding study for three commonly used industrial collectors: ethyl xanthate [$CH_3CH_2OCS_2^-$ (EX) and its oxidised disulphide form $(CH_3CH_2OCS_2)_2$, $(EX)_2$], N,N-diethyl dithiocarbamate [$(H_5C_2)_2NCS_2^-$, DEDTC] and diisobutyl dithiophospinate [$(H_{10}C_4)_2PS_2^-$, DTPi] (see Figure 1), as well as for OH^- and H_2O which can bind competitively to mineral surfaces. The minerals investigated were sperrylite ($PtAs_2$, Sp) and pentlandite [$(Fe,Ni)_9S_8$, Pn], which are often present together in froth flotation separations, and platinum (Pt), included in this work to serve as a reference for sperrylite due to strong similarities in both physical and chemical properties. We then report results obtained from cyclic voltammetry measurements undertaken for the three collector ligands in the presence of working electrodes made from Sp, Pn and Pt, and compare the results obtained with the hierarchy of ligand/surface binding strengths obtained in the computational study.

2.0. Experimental and Computational Methods

Computational Modelling: All calculations were carried out using the plane-wave DFT code CASTEP 7.02 and CASTEP 8.0,[17] utilizing the PBE[18] exchange-correlation functional, ultrasoft pseudopotentials generated 'on the fly' and a plane wave basis set expressed to a cut-off of 550 eV, which demonstrated convergence for all models to within 0.2 meV/atom. K-point sampling grids, generated using the Monkhorst-Pack scheme,[19] were chosen for each model such that sampling intervals were no greater than 0.05 $Å^{-1}$. Experimental measurements report Pn to be non-magnetic[20] which carries the implication of net zero spin, however the possibility of an antiferromagnetic spin polarised state cannot be ruled out. Finding this state is far from trivial, however, given the complexity of Ni/Fe disorder, combined with the variation in possible oxidation state and spin state for each of the metal sites. To this end, all calculations reported relate to spin-restricted wavefunctions and we have not pursued the use of DFT+U functionals[21-22] which are known to be important for correcting the over-delocalisation of electrons observed in condensed matter transition metal systems by pure DFT functionals,[23] and are thus important in work where in-depth knowledge of the oxidation states and spin states is sought. The issue of site disorder in Pn was addressed by us in an earlier publication.[24]

Crystallographic data were accessed through the MINCRYST[25] database, and subjected to atom-only minimisation (convergence tolerances for force, ionic displacement and energy were 0.05 eV $Å^{-1}$, 0.001 Å and 0.01 meV/atom, respectively). The vacuum height for all surface-only models was set at 10 Å, which increased to at least 15 Å upon surface binding of collector ligands. The optimal slab depth for each mineral surface varied. Full documentation regarding the construction of the surface models for Sp and Pt is available in the electronic supplement S1; data regarding the construction of the surface model for the disordered mineral Pn are available in an earlier publication.[24]

In order to limit lateral inter-ligand interactions, a 2×2×1 supercell representation of the Sp surface was used to study collector ligand binding. This model presented eight surface Pt metal atoms, representing ¼ coverage when a single EX^- ligand binds in a bridging motif. To accommodate binding of the (EX_2) ligand, the surface model was increased further to a 3×2×1 representation, and the ligand docked such that its longest direction was positioned parallel to the long **a**-vector surface repeat. For Pt the [111] surface (which had previously been reported as the most cleavage plane),[26] was used throughout in this work, with a 3×3×1 representation employed for the smaller collector ligands EX and DEDTC (representing four

exposed metal atom sites per unit cell, and therefore approximately ½ coverage upon adsorption of one bridging EX ligand), increasing to a 4×4×1 representation for the larger ligand DTPi and for the water monolayer study, whilst $(EX)_2$ surface binding required a 5×5×1 representation. For Pn, a 1x1x1 surface unit cell, as defined in our previous work,[24] was sufficient to model the smaller ligands. This surface model presents four surface metal atoms (either Fe or Ni), and so binding of a single bridging EX ligand represents ½ surface coverage. A 2x2×1 supercell representation was used for the larger ligands DTPi and $(EX)_2$.

Throughout this work models for the adsorbed ligand-plus-surface, surface-only and ligand-only are referenced by $[L+S]$, $[S]$ and $[L]$ respectively, with superscript numbers representing any charged states where appropriate. In these simulations, ligands are bound to one surface only, which raises the possibility that the $[L+S]$ models carry a dipole. However, the dipole correction to the total energy, as calculated using the Neugebauer and Scheffler[27] scheme is small, typically less than *ca.* 10 meV per unit cell (see electronic supplement, S1).

Geometry optimisations for EX^-, $DEDTC^-$, $DTPi^-$ and OH^- were performed using a series of cubic unit cells of increasing size from $20-40$ Å at 5 Å intervals. The total energies of these models were corrected with a simplified Makov-Payne correction[28] scheme to negate the slow convergence of the electrostatic energy with increasing unit cell size for charged systems (see electronic supplement S2 for full details). Total energies were seen to converge to *ca.* 0.01 eV using a periodic boundary condition box of **a** = 40 Å; for OH^- geometry optimisations failed to converge using box sizes greater than 30 Å, and so convergence with respect to box size is limited to 0.08 eV for this ligand. For the neutral ligands H_2O and $(EX)_2$ convergence of the total energy with unit cell size is rapid, and so a smaller unit cell was used in this case (**a** = 20 Å).

The binding energy (E_B) of a non-charged ligand to a surface can be found simply as the difference in total energy between the neutral ligated surface ($[L+S]^0$) and the sum of the neutral ligand-only ($[L]^0$) and neutral surface-only ($[S]^0$) models, as expressed in Equation 4.

$$E_B = [L+S]^0 - ([L]^0 + [S]^0) \qquad (4)$$

This equation holds assuming that the atom and electron counts for $[L+S]^0$ and $([L]^0 + [S]^0)$ are the same. However, if $[L]$ carries a formal negative charge electron balance will only be maintained if $[L+S]$ also carries a negative charge. This presents a problem, as the periodic boundary condition box sizes required to demonstrate effective energy convergence will be prohibitively large. To this end, we recently proposed a solution[24] whereby the total energy of the $[L+S]^-$ system can be replaced by $[L+S]^0$ provided a correction for the extra electron in the electronic band structure is taken into account. This correction is the surface work function, ϕ. In this work we have calculated this correction for the $[L+S]$ system, which represents a step forward from our earlier publication where the correction was derived from the bare surface model $[S]$. Full details are recorded in electronic supplement, S1. In this way the binding energy of a charged ligand $[L]^-$ to a neutral surface $[S]^0$ can be calculated using the following expression:

$$E_B = ([L+S]^0 - \phi_{[L+S]^0}) - ([L]^- + [S]^0) \qquad (5)$$

Cyclic voltammetry (CV): Cyclic voltammetry was performed using a conventional three electrode cell with specially constructed Sp and Pn mineral working electrodes (electronic supplement S3), and a Pt-wire working electrode. A Pt-gauze counter electrode was used throughout and the cell potential was measured against a saturated calomel electrode, with a standard S.H.E. potential correction of +0.244 V. Experiments

were performed in quiescent, Ar degassed, 0.05 M sodium tetraborate buffer solution (pH 9.2) prepared fresh daily using commercially available tetraborate buffer tablets and deionised water with a final resistivity of 18.2 $M\Omega cm^{-1}$. Ar was passed over the cell during experiments to prevent return of atmospheric oxygen to the solution. Voltammograms were recorded using a Metrohm Autolab Pgstat 12 potentiostat at a scan rate of 10 mVs^{-1}. Potential ranges varied for each working electrode as outlined below.

For the mineral working electrodes, fresh electrode surfaces were produced prior to each experiment by wet abrasion of the electrode face with increasing grits of silicon carbide abrasive paper, starting at 600 grit and rising to 1200 grit, for five minutes each for a total of ten minutes of polishing time per experiment. Particulate matter was washed from the electrode face with deionised water and the electrode immediately transferred into the cell to limit surface oxidation. The Pt working electrode was cleaned by rapid electrochemical cycling in a 0.1 M H_2SO_4 solution between -0.4 V and +1.2 V *vs.* S.H.E.

EX and DEDTC were purchased as their potassium salts, whilst DTPi was provided as a 50% w/w solution by Cytec Solvay Group under the tradename AEROPHINE ® 3418A Promoter. Solution concentrations of 1×10^{-3} M for each was achieved by appropriate volumetric addition via auto-pipette to the tetraborate buffer solution. Prior to the addition of collector ligands the potentiostat was engaged and the cell held at -0.4 V *vs*. S.H.E. to prevent spontaneous oxidation of collector ligands at the mineral surface. After ligand addition, the cell was degassed with Ar for a further 5 minutes to allow for better ligand dispersion into the gas-agitated solution, and to provide ample time for ligand chemisorption and/or surface complex formation.

Initial voltammetry was performed to establish a safe protocol under which each mineral working electrode could be operated without incurring surface oxidation and possible leaching of arsenic (in the case of Sp) and sulfur, Fe and Ni (in the case of Pn), with data reported in electronic supplement S4. Safe potential ranges of -0.4 V to +0.6 V *vs.* S.H.E. for Sp and -0.4 V to +0.4V *vs.* S.H.E. for Pn were found which limited surface degradation. As surface oxidation would significantly affect adsorption, voltammogram results for ligands on all working electrodes were only assessed for the first cycle. The Pt wire working electrode required much less stringent handling, and the response to the potential range -0.4 to +0.8 V was explored.

3.0 Results and Discussion

3.1 Computational surface models.

Images representing the working surfaces defined for Sp, Pn and Pt are displayed in Figure 2. For Sp, cleaving the crystal lattice along the low Miller Index (MI) planes [100], [110] and [111] generated a total of 11 different surface terminations (see electronic supplement S1). However of these only one model for each MI plane retains the bulk stoichiometric ratio, a requirement for calculating the surface energy.[29] Total energies, surface energies and reference literature values for the three quantifiable surface models, optimised with a slab depth of ca. 15 Å (corresponding to a 4-layer slab model) are documented for Sp in the electronic supplement S1. From this it is readily apparent that the [100] surface is the most stable (surface relaxation energy equal to 1.01 Jm^{-2}), followed by [110] and [111] (with surface relaxation energies of 1.62 and 2.50 Jm^{-2}, respectively), and the trend observed is in line with literature values.[26] We note also that DFT modelling appears to suggest that the cleaved surfaces for Sp are more stable than was reported by earlier (classical interatomic potential) modelling work.[30]

For the disordered mineral Pn, initially treating all metal sites as equivalent and cleaving along the [100], [110] and [111] MI planes yields a total of thirteen possible symmetric surface models,[24] however of these only one, created by the [111] cut, retains the bulk (Fe,Ni):S ratio which permits its surface relaxation

energy to be quantified [Figure 2(b)]. From our earlier study on Pn, [111] surface energies fall into the range 1.13 – 1.38 Jm^{-2}, based on a set of ten randomly explicitly defined bulk models and a lowest energy bulk model found via a cluster expansion Hamiltonian approach.[24] In our earlier publication we suggested that the issue of metal site disorder could be addressed by the construction of two extreme models: one where all metal surface atoms are defined to be Fe (labelled Fe-Pn) and another where all metal surface atoms are defined to be Ni (labelled Ni-Pn). The rest of the sub-surface metal atoms (expressed to five atomic layers, representing a slab depth of *ca*. 12 Å) are then randomly assigned to either Ni or Fe while maintaining the Ni:Fe ratio of 1:1 overall. Results from these two models allow an upper and lower bracket for a ligand binding energy range to be calculated.

Finally, for pure Pt the literature points to cleavage along the [111] MI plane as giving rise to the most stable surface model [see Figure 2(c)],[26] and this was used without independent verification in this work. Varying the slab depth from 3 to 15 layers returned values for surface energies that eventually converged to 1.46 Jm^{-2} (see electronic supplement S1), which compares well with the literature value of 1.49 Jm^{-2} reported for similar DFT calculations.[26] As a trade-off between calculation accuracy and speed, a slab depth of 5 layers (corresponding to *ca.* 10 Å, and a surface energy of 1.50 Jm^{-2}) was adopted in this work.

As outlined above, a correction to account for the extra electron introduced into the mineral surface band structure upon binding an anionic ligand was obtained by calculating the surface work function, $\phi_{[S]^0}$ for each of the bare slab models. The results of this process for the working surfaces just defined are presented in full in the electronic supplement S1.

3.2 Surface + Ligand models.

3.2.1 EX on Sp, Pn and Pt

Two models for EX adsorption on Sp were obtained: (i) monodentate, with only one S atom on the xanthate anion attached to a surface Pt, and (ii) bridging, with each S atom on the xanthate anion addressing a different Pt atom in the surface cleft, as shown in Figure 3. Note attempts to model a bidentate interaction, where both S atoms addressed the same Pt ion on the surface fell into a bridging minimum where the ligand straddled Pt and As ion sites. As this structure was considerably less energetically favourable than the models where the ligand binds to Pt only it was not pursued any further.

From the associated binding energies (Table 1) it is readily apparent that the bridging geometry is significantly more favourable than the monodentate geometry (by *ca.* 70 kJ mol^{-1}). From Figure 3(b) it is apparent that when bridging two metal sites the EX ligand twists (ca. 13° around the O–C bond) to fit within the surface cleft more readily, and analysis of the electron localisation function (ELF) plot [Figure 3(c)] indicates this distortion minimises the steric repulsion between the As and S lone pairs. Thus, if the [100] Sp surface is an accurate representation of the actual surface of Sp particulate matter, it is apparent that any successful collector ligand will have to present a narrow anionic head group to the [100] Sp surface to circumnavigate the electronic steric crowding effect of the surface As sites.

Surface adsorption of EX onto Pn was discussed in full in our earlier paper,[24] but results with an updated surface work function correction (based on $\phi_{[L+S]^0}$) are presented here in Table 1. Only one adsorption site, where the EX ligand bridges two metal atoms in the surface was located, and it is apparent that the collector ligand binds more strongly to the Fe-rich surface than to the Ni-rich surface, with the former returning a binding energy *ca.* -100 kJ mol^{-1} stronger than the latter, which in turn is still *ca.* -80 kJ mol^{-1} stronger than the binding energy of EX to Sp. Benchmark comparison figures for Fe-S surface interactions

are available from DFT simulations on the adsorption of atomic sulfur on Fe(110), which suggested binding energies in the region of -350 to -575 kJ mol^{-1}, depending on surface coverage and binding site,[31] which offers confidence in the values obtained in this work.

Three adsorption models were pursued for surface adsorption of EX to Pt. For each, one S ligand atom was held over the top of one Pt atom, and the ligand rotated until the second S atom sat either above another Pt (OnOn), or above an HCP hollow site (OnHCP) or above an FCC hollow site (OnFCC), as shown in Figure 4. The calculated total binding energies lie in a narrow range from -499.8 to -505.6 kJ mol^{-1}, much stronger than the total binding energy of EX to any of the other surfaces investigated in this study, which is logical given the pure nature of this surface. The strong binding can also probably be attributed to the idealised nature of the Pt surface, which is geometrically flat and free from attendant lone pairs from other associated elements that can act to distort the ligand geometry.

$(EX)_2$ was also modelled on the three surfaces, as the oxidative dimerization reaction of EX (and subsequent ligand rearrangement involving cleavage of some M-S bonds) forms the basis for experimental validation of predicted collector ligand/surface binding energies by the cyclic voltamogram measurements. $(EX)_2$ can adopt *cis* and *trans* conformations with respect to the central S-S bond, and while *trans*-$(EX)_2$ is the more stable configuration (by 9 kJ mol^{-1}, see electronic supplement S2), *cis*-$(EX)_2$ offers more efficient surface coverage through the presentation of two C=S groups, rather than one. However, upon attachment to the surface, the latter dissociated back to monomers in a process that introduced significant surface distortion, and so this binding motif was not pursued any further. The results obtained for the *trans* configuration are reported in Table 1 and Figure 5, and support weak binding of -51.5 kJ mol^{-1} to the Sp surface. $(EX)_2$ also appears to bind weakly to the Pn and Pt surfaces, [-128.8 (Fe-Pn), -62.5 kJ mol^{-1} (Ni-Pn)] and to Pt (-126.3 kJ mol^{-1}). The binding distances (documented in electronic supplement S3), are greater for $(EX)_2$ than for the bridged form of EX, which is consistent with the suggestion that $(EX)_2$ is present as weakly bound physisorbed layers, while EX chemisorbs strongly to mineral and metal surfaces. The modelling work therefore appears to support the hypothesis that binding of the xanthate dimer to the mineral surfaces results in the cleaving and weakening of M-S bonds compared to surface binding of the monomer state.

3.2.2 DEDTC and DTPi on Sp, Pn and Pt

DEDTC and DTPi were presented to Sp, Ni-Pn and Fe-Pn surfaces as bridging ligands, as this had already been established as the most favourable mode of binding for the structurally analogous EX anion. Likewise for the Pt surface, the three binding sites already identified [as defined in Figure 4(a)] were utilised again to investigate DEDTC and DTPi binding. Output geometries for all models are presented in Figures 6 and 7, and associated binding energies in Table 2.

The first point to note is that all ligand systems bind to all surface models, and stable structures were reported in every case. Steric interference on the mineral surfaces appears not to obstruct ligand binding, even for the bulky DTPi anion. A clear trend emerges from the data: all ligand systems bind most weakly to Sp, followed by Ni-Pn and Fe-Pn respectively, with the highest binding energies observed for Pt. For the Pt surface, there is little variation in the binding energies obtained for the different binding sites, and it is hard to identify any consistent trend for variation with collector ligand identity, which suggests that, for a homogenous atomically flat surface the bulk of the ligand interaction stems from the sulphur head group atoms, as might be expected.

Binding energies for DEDTC are comparable to those for EX for all surface models, which also suggests that binding to the surface models is defined by to the $–CS_2$ unit. This head group undergoes a significant twist around the N–C bond [of ca. 13°, Figure 6(a)] to permit attachment to the rippled surface of Sp, compared to the atomically flatter Pn [Figures 6(b)-(c)]. However, on the completely flat Pt surface the availability of many possible binding sites [Figures 6(d)-(f)] can induce a twist of up to 22°, and the pattern of ligand attachment changes from a simple bridging motif to a tridentate arrangement.

Greater variation is observed in the binding energies of DTPi to the four surface models. Significantly lower binding energies are observed for Sp and Fe-Pn. From Figure 7(a) it is tempting to attribute this to greater steric repulsion with the mineral surface, with the hydrocarbon arms more likely to come into contact with As lone pairs on the Sp surface ridges, and a simple comparison of the $Pt–S_{ligand}$ distances reveals that this ligand appears to rest further away from the Pt binding sites than for other collector ligands (electronic supplement S3). It is also apparent that replacing the $-CS_2$ head group with $-PS_2$ gives rise to a much more flexible docking ligand, with S···S distances able to span a range of up to 3.6 Å, compared to 3.1 Å for the more rigid EX and DEDTC ligands. For the Pt surface, attachment to the 'OnOn' binding site resulted in dissociation of the ligand, so binding energies are reported in Table 2 for the 'OnFCC' and 'OnHCP' only; energies are comparable to those observed for DEDTC to Pt.

3.2.3 H_2O and OH^- on Sp, Pn and Pt

To account for the effects of solvation accurately in the computational study the vacuum layers in the surface models should be populated with an appropriate number of explicitly-defined water molecules. However, this would render the task of geometry optimisation extremely computationally demanding, and with so many degrees of freedom, an increasingly complex task that would necessitate the need to shift to a molecular dynamics approach. In an alternative effort to account for some of the effects of solvation at the most basic of levels, the surface models investigated in this study were presented with partial and full mono-layers of H_2O. Partial OH^- adsorption was also considered. Optimised geometries for Sp, Ni-Pn, Fe-Pn and Pt models are reported in Figures 8 - 10, along with binding energies in Table 3 and structural information in electronic supplement, S3.

Results show that at low surface coverage, the plane of the H_2O molecule adopts a position almost parallel to the surface in all models. This observation is in keeping with reports for other surfaces.[32-33] However for Sp the raised As ridges prevent a fully parallel binding geometry from being obtained. The low reported binding energy (-21.5 kJ mol^{-1}, Table 2), along with a relatively long Pt–O bond (2.48 Å) suggests H_2O binds weakly to Sp. Introducing a second H_2O molecule, to create a full monolayer model, gives a significantly different optimised structure [Figure 8(b)]. The second H_2O molecule has flipped into a 'hydrogen down' geometry with a Pt…H distance of 2.76 Å. This weak interaction is compensated by the formation of a hydrogen bond with the first H_2O molecule, which increases the overall average binding strength per molecule (see Table 3). The full monolayer binding energy of -29.0 kJ mol^{-1} per molecule is in good agreement with the literature value of -27.1 kJ mol^{-1} calculated by Ntoahae[34] using LMTO DFT. The geometries do not appear to be consistent however, with the LMTO DFT study appearing to retain the Pt–O bond and no obvious hydrogen bonding interactions between molecules is apparent. It is therefore likely that the weakly-bound hydration layer on Sp is mobile, with hydrogen bonding and Pt–O interactions acting in competition. Note dispersion interactions (not included in the pure PBE functional used in this work) may increase the strength of ligand binding.

From the data presented in Table 3 it is apparent that water binds more strongly to Pn than Sp, and shows a greater affinity for Fe than for Ni. The Fe-terminated surface is more uneven than the flatter Ni-

terminated slab, which has a knock-on impact on the network of hydrogen bonding that can exist between water molecules bound in a monolayer arrangement (see Figure 9). There are several calculations reported in the literature that can be used to assess the results we obtained here. Firstly, simulations have been reported for the adsorption energies of H_2O on pure Ni and Fe surfaces. The Ni–OH_2 adsorption energy on the Ni(110) face (the only low MI face that is not atomically flat, and so presents a surface somewhat similar to Ni-Pn) is -45.1 kJ mol^{-1}, as determined by Mohsenzadeh et al,[35] which is in good agreement with our higher surface coverage binding energies (ca. -45.5 kJ mol^{-1}). For Fe, only H_2O adsorption energies for the atomically flat Fe(110) surface have been reported, and their adsorption energy of -36.5 kJ mol^{-1} falls somewhat short of the ca. -65 kJ mol^{-1} found in this study.[36] However, values for the adsorption of H_2O on the ridged (100) surface of pyrite (FeS_2, which is isostructural with Sp) using DFT have been reported by two other groups: Zhao[37]and Stirling[38] report binding energies of -71.2 and -54.1 kJ mol^{-1}, respectively, which do compare favourably with the data reported in this study.

The adsorption of H_2O on the Pt(111) surface is amongst one of the most well studied surface systems, both computationally[39-41] and experimentally[42-44]. In this study we have pursued the flat ice monolayer structure, identified experimentally by Ogasawara,[44] and in addition we have also modelled the adsorption of a single H_2O molecule on the on-top and bridge sites. Figure 10 shows the output geometries for all three models. The calculated on-top monomer binding energy of -32.1 kJ mol^{-1} (see Table 3) is in good agreement with that calculated by Meng (-29.1 kJ mol^{-1}),[40] while agreement for binding to the bridge site fares less well (-5.6 vs -11.2 kJ mol^{-1}). However, data obtained for the flat ice structure does compare well with prior work (average binding energy per H_2O of -48.0 kJ mol^{-1}, *c.f.* Meng *et al*. -51.3 kJ mol^{-1}) and also shows that this is the preferred hydrated state, with hydrogen bond interactions between water molecules acting to stabilise the monolayer structure.

For OH^- binding to the Pt surface, the charged ligand was presented 'oxygen down' on the on-top, bridge, FCC and HCP three-fold hollows. However the latter two collapsed to the bridge and on-top minima, respectively, as shown in Figure 8. Analysis of the binding energies suggests that, whilst the bridging geometry bonds to two surface metals (with rPt–OH = 2.14 Å), and the on-top geometry binds to only one (rPt–OH = 1.97 Å), they have similar total energies (ca. -570 kJ mol^{-1}). From the literature we note the work by Lew,[45] who reported the adsorption enthalpy of Pt–OD (from the breakdown of D_2O via a radical process on Pt surfaces already doped with O) using microcalorimetry (ca. -270 kJ mol^{-1}), matched with a corresponding DFT calculation confirming an adsorption energy of -280 kJ mol^{-1}. We note that the difference in calculated binding energies between that study and ours is entirely due to the treatment of the negative charge in OH^-. Treating OH as a neutral radical and recalculating our binding energies give values of the order of -300 kJ mol^{-1}, in reasonable agreement with Lew's values. We also note the work by Marković[46] and Mooney,[47] who also cite Pt–OH bond enthalpies derived via radical formation and quote values in the region of -136 and -235 kJ mol^{-1}, respectively. Assuming a radical process is also involved in the adsorption of hydroxide to Sp and Pn, we provide the corresponding radical-process binding energies for all calculated surfaces in Table 3. It is interesting to observe that these energies obtained are now comparable to the binding energies obtained for the collector ligands quoted in Tables 1 and 3.

The data in Table 3 indicate that Pn binds H_2O more favourably than Pt or Sp, and, taken in conjunction with the data presented in Tables 1 and 3, it would be energetically favourable to desolvate an entire monolayer of water from all of the surface models to allow any one of the collector ligands to adsorb. For hydroxide adsorption, assuming a radical process, the modelling work predicts binding energies that are comparable to the collector ligands, and the absolute values for the binding energies rise considerably if the ligand is treated as an anion. Note however, solvation effects, both of the surface models and of the

ligands, would be expected to influence results considerably. These results also point to the need for future work to move beyond the idealised surfaces used herein to study oxidised surfaces, which may alter the trends that have emerged in this work. However, the general observation that hydroxide binding competes with collector ligand binding is likely to remain, and supports the importance of chemical modifiers used in the froth flotation process to control pH conditions.

3.3 Validation of modelling trends – electrochemistry measurements

3.3.1 EX on Sp, Pn and Pt

First-cycle voltammograms for Sp, Pn and Pt working electrodes in the presence of $1x10^{-3}$ M potassium ethyl xanthate (KEX) are presented in the electronic supplement, S4, alongside voltammograms recorded in the absence of collector ligand. All three working electrodes show a passivation of current, indicating that ligand binding is taking place and all show an oxidation peak for the dimerization reaction beyond the equilibrium potential for $2EX^-/EX_2$ couple (0.121 V at a concentration of $1x10^{-3}$ M).[48] While the shapes of the Sp and Pt voltammograms show clear diffusion limited behaviour, the need to limit the oxidation potential to no greater than 0.4 V for Pn curtails the full development of this peak in the voltammograms recorded for this electrode.

Direct comparison of voltammograms for the three electrodes is difficult as the electrode surface area, and hence the charge passed, vary due to electrode design factors. To counter this, voltammograms were normalised to the highest current registered in the region 0 to +0.5 V (where ligand oxidation occurred) in the forward trace and all other currents scaled relative to this (plots are shown in supplementary information, S4). As not all the electrodes displayed clear diffusion limited peaks, the steepest point of the oxidation trace is the most reasonable indicator of the equilibrium redox potential. This can be found by differentiating the current in each trace with respect to potential to give the plot shown in Figure 11(a). A clear progression can be observed for the oxidation potentials of EX on the three working electrode surfaces, and the peak maxima show good agreement with mixed oxidation potentials quoted by others (Sp (ca. +0.26 V vs SHE,[6] Pn ca. +0.24 V vs SHE,[49] along with Pt ca. 0.4 V vs SHE[3]). The progression of mixed oxidation potentials therefore offers qualitative insight into the strength of ligand binding, provided of course that the assumption of oxidation of ligands chemisorbed to the mineral and metal surfaces holds. The order recorded (Sp < Pn < Pt) matches the order of calculated binding energies for EX to the mineral surfaces, as presented in Table 1.

3.3.2 DEDTC and DTPi on Sp, Pn and Pt

First-cycle voltammograms for Sp, Pn and Pt working electrodes in the presence of $1x10^{-3}$ M N,N-diethyl dithiocarbamate (DEDTC) are presented in the electronic supplement, S4. Note the equilibrium potential for DEDTC/$(DEDTC)_2$ for the given concentration is not reported in the literature, but it is reasonable to assume that the current increase observed above 0.15 V is due to the dimerization reaction.

As with the EX measurements, clear diffusion-limited peaks were observed on Sp and Pt, and again for the Pn electrode the upper oxidation limit prevents full peak formation. Normalising the data, and differentiating the current with respect to the potential yielded the plot shown in Figure 11(b), from which a number of key points are apparent. Discarding the incomplete data set for Pn, for which no clear spike in the current is apparent, we observe that the peak ordering compared to the data presented for EX (i.e. Sp < Pt) has been preserved, and this again matches the predicted trend from the computational modelling. Also

of note is the observation is that the peak maximum recorded for the Pt electrode shifts to the left whilst that for the Sp electrode shifts to the right, implying that DEDTC requires weaker oxidising conditions to induce the formation of the disulphide on Pt but stronger on Sp. This may carry the underlying implication that this ligand must bind more weakly to Pt and more strongly to Sp, compared to EX. Interestingly, this trend is apparent in the computational modelling data, but given the limitations that are present in the computational work (idealised surfaces free from the effects of surface oxidation, solvent effects *etc*.) care must be taken not to over interpret the results obtained.

Voltammograms for DTPi do not show good diffusion limited peaks, however evidence of increased current where oxidation would be expected is observed (electronic supplement, S4). The redox potential of DTPi has not been quantified but Woods *et al* reported an aniodic wave in the voltammogram for DTPi in the presence of a Pt working electrode at about 0.5 V.[13] In broad terms the results from the DTPi electrochemical measurements show a similar mixed oxidation potential (ca. +0.32 V) for Sp and Pn, while a higher potential (ca. +0.55 V) is required for Pt [see Figure 11(c)]. These results therefore suggest that DTPi oxidation occurs at a slightly lower potential on Sp and Pn and at a slightly higher potential on Pt, compared to the other collector ligands EX and DEDTC. If the oxidation potentials are indeed reflecting the underlying strength of monomer ligand binding then the correlation with the computational ligand binding strengths is a little mixed: DTPi was predicted computationally to bind more strongly to Pt than to any other surface but by a very small margin, and more weakly to Pn (notably Fe-Pn), but binding to Sp falls in the middle of the range of calculated binding energies. It is likely that the reasons for the discord lie in the low quality of the experimental data obtained, along with the above-mentioned limitations in the modelling work.

4.0 Conclusions

This study documents a combined computational and experimental investigation into the binding of ethyl xanthate, N,N-diethyl dithiocarbamate and diisobutyl dithiophosphinate to sperrylite, pentlandite and platinum. Surface modelling work focused on the most stable quantifiable surface models for the two minerals, which were generated by cleaving along the [100] MI plane for sperrylite and [111] MI plane for pentlandite, along with a [111] MI surface model for pure platinum. Work surface functions were calculated for all models to permit application of an energy correction terms to counter the effects of the negative charge introduced by anionic ligands, which would otherwise give rise to unreliable Coulombic energy summations under periodic boundary conditions. The first principles modelling work showed a clear trend for all three collector ligands to bind least strongly to the platinum-containing mineral sperrylite, followed by the mixed nickel/iron mineral pentlandite, while all ligands showed strongest binding affinity for the pure platinum surface. Geometry optimisation calculations also supported the literature experimental observations that the oxidised (disulphide) form of ethyl xanthate binds much more weakly to all surface models than the monomer state. A monolayer of water molecules would easily be displaced from all surfaces by any of the collector ligands, but the same does not hold true for the hydroxide anion, which was found to have binding energies of comparable magnitude to the collector ligands.

Cyclic voltammetry performed on working electrodes constructed from sperrylite, pentlandite and platinum permitted measurement of the mixed oxidation potential associated with the generation of the disulphide forms of all three collector ligands, although less clear cut data was obtained for diisobutyl dithiophosphinate and N,N-diethyl dithiocarbamate on pentlandite. Assuming that the mixed potentials give a direct measure of the strength of monomer ligand binding to the different surfaces, comparing the relative ordering of the mixed potentials obtained for the collector three ligands on sperrylite, pentlandite and platinum provides a route to experimentally validate the computational study. In general a favourable match with the predicted binding energy strengths was obtained, indicating that for these minerals and

collector ligands a correlation does exist between the mixed oxidation potential and the ligand/mineral binding energy.

This benchmark study has demonstrated that first principles simulations can be used to predict the binding energies of collector ligands to mineral and metallic surfaces. It could therefore be applied in a predictive manner to screen other ligands for favourable binding energies, and to identify ligands which show selective binding to one mineral over another. That said, the froth flotation process is complex, and predicting strength of ligand binding will not translate in a straightforward manner to a measure of the flotation outcome, which is influenced by a large number of other chemical, physical and operational factors including the addition of other surface active species *etc.* which are likely to accumulate at the interface to which mineral particles adhere. Several studies have investigated the poor flotation properties of sperrylite and cite particle size and size distribution, along with potential interactions with other sulfur-containing species which may interact with the sperrylite grains and so depress its flotation properties.[6] In addition it is worth remembering that the modelling work documented here was performed on pristine, idealised surface models of minerals and metal surfaces. In reality, complex oxidation behaviour is likely to occur, which can reasonably be expected to be condition-dependent and give rise to significant alterations to the surface chemistry. It is clear that further experimental exploration is needed, but it is also clear that computational modelling studies also have an important role to play in this field.

Acknowledgements

C.N.W. gratefully acknowledges CYTEC Industries Inc. and Anglo American Plc. for the award of a Ph.D. studentship, along with the UK Carr Parrinello consortium for allocation of computing time on the EPSRC high performance computing resource ARCHER (managed by the Edinburgh Parallel Computing Centre, EPCC), along with the EaSTCHEM Research Computing Facility and the University of Edinburgh ECDF facility. We also acknowledge Dr. Phil Hasnip (University of York) and Mr. Thomas R. Durrant (University College London) for helpful insights on charged periodic boundary condition models within CASTEP, and Dr. Damien Corrigan (University of Edinburgh) for invaluable guidance with the electrochemistry measurements.

Supporting Information for Publication

Computational modelling: deriving models for the mineral working surfaces and isolated ligands. Electrode construction and performance. Electrochemical data.

REFERENCES

1. Kelly, E. G.; Spottiswood, D. J., *Introduction to Mineral Processing*; Wiley, 1982.
2. Nagaraj, D. R.; Ravishankar, S. A., Floatation Reagents - a Critical Overview from an Industry Perspective. In *Froth Flotation: A Century of Innovation*, Society for Mining, Metallurgy, and Exploration: 2007.
3. Woods, R., Oxidation of Ethyl Xanthate on Platinum, Gold, Copper, and Galena Electrodes. Relation to the Mechanism of Mineral Flotation. *J. Phys. Chem.* **1971**, *75*, 354-362.
4. Bozkurt, V.; Xu, Z.; Finch, J. A., Pentlandite/Pyrrhotite Interaction and Xanthate Adsorption. *Inter. J. Min. Proc.* **1998**, *52*, 203-214.
5. Pecina, E. T.; Uribe, A.; Nava, F.; Finch, J. A., Mechanism of Di-Isobutyl Dithiophosphinate Adsorption onto Galena and Pyrite. *Miner. Eng.* **2006**, *19*, 904-911.
6. Vermaak, M. K. G.; Pistorius, P. C.; Venter, J. A., Fundamental Electrochemical and Raman Spectroscopic Investigations of the Flotation Behaviour of $Ptas_2$. *Miner. Eng.* **2007**, *20*, 1153-1158.
7. Vermaak, M. K. G.; Miller, J. D.; Lee, J., Electrochemical Interactions of Industrially Important Platinum-Containing Minerals. *Miner. Eng.* **2007**, *20*, 1337-1343.
8. Vermaak, M. K. G.; Pistorius, P. C.; Venter, J. A., Electrochemical and Raman Spectroscopic Studies of the Interaction of Ethyl Xanthate with Pd–Bi–Te. *Miner. Eng.* **2005**, *18*, 575-584.
9. Woods, R.; Hope, G. A.; Brown, G. M., Spectroelectrochemical Investigations of the Interactions of Ethyl Xanthate with Copper, Silver and Gold: Iii. Sers of Xanthate Adsorbed on Gold Surfaces. *Colloids and Surfaces A: Physiochem. Eng. Aspects* **1998**, *137*, 339-344.
10. Mermillod-Blondin, R.; Kongolo, M.; de Donato, P.; Benzaazoua, M.; Barrès, O.; Bussière, B.; Aubertin, M., Pyrite Flotation with Xanthate under Alkaline Conditions — Application to Environmental Desulfurisation. In *Centenary of Flotation Symposium*, Brisbane, Australia, 2005.
11. Venter, J. A.; Vermaak, M. K. G., Dithiocarbonate and Trithiocarbonate Interactions with Pyrite. *South African Journal of Science* **2007**, *103*, 164-168.
12. G. A. Hope; R. Woods; G. K. Parker; K. M. Watling; Buckley, F. A., Spectroelectrochemical Investigations of Flotation Reagent-Surface Interaction. *Minerals Engineering* **2006**, *19*, 561-570.
13. G. A. Hope; R. Woods; Watling, K., A Spectroelectrochemical Investigation of the Interaction of Diisobutyldithiophosphinate with Copper, Silver and Gold Surfaces: Ii. Electrochemistry and Raman Spectroscopy. *Colloids and Surfaces A: Physiochem. Eng. Aspects* **2003**, *214*, 87-97.
14. G. D. Senior; Trahar, W. D., The Influence of Metal Hydroxides and Collector on the Flotation of Chalcopyrite. *Inter. J. Min. Proc.* **1991**, *33*, 321-341.
15. M. Tadie; K. C. Corin; J. G. Wiese; M. Nicol; O'Connor, C. T., An Investigation into the Electrochemical Interactions between Platinum Group Minerals and Sodium Ethyl Xanthate and Sodium Diethyl Dithiophosphate Collectors: Mixed Potential Study. *Miner. Eng.* **2015**, *83*, 44-52.
16. Sholl, D. S.; Steckel, J. A., *Density Functional Theory: A Practical Introduction*; J. Wiley & Sons: Hoboken, NJ, 2009.
17. Clark, S. J.; Segall, M. D.; Pickard, C. J.; Hasnip, P. J.; Probert, M. J.; Refson, K.; Payne, M. C., First Principles Methods Using Castep. *Z. Kristallogr.* **2005**, *220*, 567-570.
18. Perdew, J. P.; Burke, K.; Ernzerhof, M., Generalized Gradient Approximation Made Simple. *Phys. Rev. Lett.* **1996**, *77*, 3865-3868.
19. Monkhorst, H. J.; Pack, J. D., Special Points for Brillouin-Zone Integrations. *Phys. Rev. B.* **1976**, *13*, 5188-5192.
20. Drebushchak, V. A.; Fedorova, Z. N.; Sinyakova, E. F., Decay of $(Fe_{1-X}Ni_x)_{0.96}S$ DSC Investigation. *J. Therm. Anal. Calorim.* **1997**, *48*, 727-734.
21. Liechtenstein, A. I.; Anisimov, A. I.; Zaanen, J., Density-Functional Theory and Strong Interactions: Orbital Ordering in Mott-Hubbard Insulators. *Phys. Rev. B.* **1995**, *52*, 5467-5470.
22. Leung, K.; Rempe, S. B.; Schultz, P. A.; Sproviero, E. M.; Batista, V. S.; Chandross, M. E.; Medforth, C. J., Density Functional Theory and Dft+U Study of Transition Metal Porphines Adsorbed on Au(111) Surfaces and Effects of Applied Electric Fields. *J. Am. Chem. Soc.* **2006**, *128*, 3659-3668.

23. Devey, A. J.; Grau-Crespo, R.; de Leeuw, N. H., Electronic and Magnetic Structure of Fe_3S_4: GGA+U Investigation. *Phys. Rev. B.* **2009**, *79*, 195126.
24. Waterson, C. N.; Sindt, J.; Cheng, J.; Tasker, P. A.; Morrison, C. A., A First Principles Study on Ligand Binding and Positional Disorder in Pentlandite. *J. Phys. Chem. C.* **2015**, *119*, 25457-25468.
25. Chichagov, A. V.; Varlamov, D. A.; Dilanyan, R. A.; Dokina, T. N.; Drozhzhina, N. A.; Samokhvalova, O. L., Mincryst: A Crystallographic Database for Minerals. *Crystallogr. Rep.* **2001**, *46*, 876-879.
26. Singh-Miller, N. E.; Marzari, N., Surface Energies, Work Functions, and Surface Relaxations of Low-Index Metallic Surfaces from First Principles. *Phys. Rev,. B.* **2009**, *80*, 235407.
27. Neugebauer, J.; Scheffler, M., Adsorbate-Substrate and Adsorbate-Adsorbate Interactions of Na and K Adlayers on Al(111). *Phys. Rev,. B.* **1992**, *46*, 16067-16080.
28. Makov, G.; Payne, M. C., Periodic Boundary Conditions in Ab Initio Calculations. *Phys. Rev. B.* **1995**, *51*, 4014-4022.
29. Stoneham, A. M., Insulator and Semiconductor Surfaces. In *Defects and Their Structure in Nonmetallic Solids*, Henderson, B.; Hughes, A. E., Eds. Springer US United States, 1975.
30. Ngoepe, P. E.; Ntoahae, P. S.; Mangwejane, S. S.; Sithole, H. M.; Parker, S. C.; Wright, K. V.; de Leeuw, N. H., Atomistic Simulation Studies of Iron Sulphide, Platinum Antimonide and Platinum Arsenide. *S. Afr. J. Sci.* **2005**, *101*, 480-483.
31. Spencer, M. J. S.; Snook, I. K.; Yarovsky, I., Coverage-Dependent Adsorption of Atomic Sulfur on Fe(110): A Dft Study. *J. Phys. Chem. B.* **2005**, *109*, 9604-9612.
32. Michaelides, A.; Ranea, V. A.; de Andres, P. L.; Kind, D. A., General Model for Water Monomer Adsorption on Close-Packed Transition and Noble Metal Surfaces. *Phys. Rev. Lett.* **2003**, *90*, 216102.
33. Carrasco, J.; Hodgson, A.; Michaelides, A., A Molecular Perspective of Water at Metal Interfaces. *Nat. Mater.* **2012**, *11*, 667-674.
34. Ntoahae, P. S. Application of Computer Simulation Methods to the Study of Platinum Group Minerals. University of Limpopo, Turfloop, South Africa, 2005.
35. Mohsenzadeh, A.; Bolton, K.; Richards, T., Dft Study of the Adsorption and Dissociation of Water on Ni(111), Ni(110) and Ni(100) Surfaces. *Surf. Sci.* **2014**, *627*, 1-10.
36. Lui, S.; Tian, X.; Wang, T.; Wen, X.; Li, Y.-W.; Wang, J.; Jiao, H., Coverage Dependent Water Dissociative Adsorption on Fe(110) from Dft Computation. *Phys. Chem. Chem. Phys.* **2015**, *17*, 8811-8821.
37. Zhao, C.; Chen, J.; Wu, B.; Long, X., Density Functional Theory Study on Natural Hydrophobicity of Sulfide Surfaces. *Trans. Nonferrous. Met. Soc. China* **2014**, *24*, 491-498.
38. Stirling, A.; Bernasconi, M.; Parrinello, M., Ab Initio Simulation of Water Interaction with the (100) Surface of Pyrite. *J. Chem. Phys.* **2003**, *118*, 8917-8926.
39. Fajín, J. L. C.; Cordeiro, M. N. D. S.; Gomes, J. R. B., Density Function Theory Study of the Water Dissociation on Platinum Surfaces: General Trends. *J. Phys. Chem. A.* **2014**, *118*, 5832-5840.
40. Meng, S.; Wang, E. G.; Gao, S., Water Adsorption on Metal Surfaces: A General Picture from Density Functional Theory Studies. *Phys. Rev,. B.* **2004**, *69*, 195404.
41. Gohda, Y.; Schnur, S.; Gross, A., Influence of Water on Elementary Reaction Steps in Electrocatalysis. *Faraday. Discuss.* **2008**, *140*, 233-244.
42. Fiorin, V.; Borthwick, D.; King, D. A., Microcalorimetry of O_2 and NO on Flat and Stepped Platinum Surfaces. *Surf. Sci.* **2008**, *603*, 1360-1364.
43. Karp, E. M.; Campbell, C. T.; Studt, F.; Abild-Pedersen, F.; Nørskov, J. K., Energetics of Oxygen Adatoms, Hydroxyl Species and Water Dissociation on Pt(111). *J. Phys. Chem. C.* **2012**, *116*, 25772-25776.
44. Ogasawara, H.; Brena, B.; Nordlund, D.; Nyberg, M.; Pelmenschikov, A.; Pettersson, L. G. M., Structure and Bonding of Water on Pt(111). *Phys. Rev. Lett.* **2002**, *89*, 276102.
45. Lew, W.; Crowe, M. C.; Karp, E.; Lytken, O.; Farmer, J. A.; Árnadóttir, L.; Schoenbaum, C.; Campbell, C. T., The Energy of Adsorbed Hydroxyl on Pt(111) by Microcalorimetry. *J. Phys. Chem. C.* **2011**, *115*, 11586-11594.
46. Marković, N. M., Effect of Temperature on Surface Processes at the Pt(111)-Liquid Interface: Hydrogen Adsorption, Oxide Formation and Co Oxidation. *J. Phys. Chem. B.* **1999**, *103*, 8568-8577.
47. C. E. Mooney; L. C. Anderson; Lunsford, J. H., Energetics for the Desorption of Hydroxyl Radicals from a Platinum Surface. *J. Phys. Chem.* **1993**, *97*, 2505-2506.
48. Woods, R.; Gardner, J. R., *Aust. J. Chem.* **1974**, *27*, 2139-2148.

49. Hodgson, M.; Agar, G. E., Electrochemical Investigation into the Flotation Chemistry of Pentlandite and Pyrrhorite: Process Water and Xanthate Interactions. . *Can. Metall. Quart.* **1989**, *28*, 189-198.

Table 1. Ligand binding energies for EX and *trans*-$(EX)_2$ on Sp, Pn and Pt, calculated as per Equation 4 for neutral species and Equation 5 for anionic species. Models relate to one ligand binding to the surface.

Surface	Ligand	Ligand charge (x)	Binding Motif	$[L+S]^0$ (eV)	$[L]^x$ (eV)	$[S]^0$ (eV)	$\phi_{[L+S]^0}$ (eV)	Total B.E. (kJ mol^{-1})
Sp	EX^-	-1	mono	-135980.10	-1677.10	-134304.43	4.54	-299.5
		-1	bridging	-135980.84	-1677.10	-134304.43	4.94	-371.3
	$(EX)_2$	0	mono	-204805.08	-3350.57	-201453.97	-	-51.5
Ni-Pn[a]	EX^- [b]	-1	bridging	-24790.12	-1677.10	-23113.15	4.10	-383.2
	$(EX)_2$	0	mono	-95805.92	-3350.57	-92454.70	-	-62.5
Fe-Pn[a]	EX^-[b]	-1	bridging	-24787.05	-1677.10	-23108.58	3.67	-485.7
	$(EX)_2$	0	mono	-95786.26	-3350.57	-92434.35	-	-128.8
Pt	EX^-	-1	OnOn	-151115.64	-1677.10	-149437.85	4.49	-499.8
			OnFCC	-151115.68	-1677.10	-149437.85	4.49	-503.7
			OnHCP	-151115.70	-1677.10	-149437.85	4.49	-505.6
	$(EX)_2$	0	mono	-418465.63	-3350.57	-415113.74	-	-126.3

[a] Ni-Pn denotes a Ni-terminated surface, Fe-Pn denotes a Fe-terminated surface.

[b] From ref 24.

Table 2. Ligand binding energies for DEDTC and DTPi on Sp, Pn and Pt, calculated as per equation 5. Models relate to one ligand binding to the surface.

Surface	Ligand	Binding motif	$[L+S]^0$ (eV)	$[L]^-$ (eV)	$[S]^0$ (eV)	$\phi_{[S]^0}$ (eV)	Total B.E. (kJ mol^{-1})
Sp	$DEDTC^-$	bridging	-136205.54	-1901.71	-134304.43	4.18	-344.6
	$DTPi^-$	bridging	-136727.37	-2424.11	-134304.43	4.47	-318.4
Ni-Pn	$DEDTC^-$	bridging	-25014.87	-1901.71	-23113.15	3.50	-338.4
	$DTPi^-$	bridging	-94877.83	-2424.11	-92454.70	4.54	-343.5
Fe-Pn	$DEDTC^-$	bridging	-25011.83	-1901.71	-23108.58	3.14	-452.2
	$DTPi^-$	bridging	-94859.06	-2424.11	-92434.35	3.82	-426.4
Pt	$DEDTC^-$	OnOn	-151340.62	-1901.71	-149437.85	3.66	-455.4
	$DEDTC^-$	OnFCC	-151340.54	-1901.71	-149437.85	3.66	-447.7
	$DEDTC^-$	OnHCP	-151340.69	-1901.71	-149437.85	3.66	-462.2
	$DTPi^-$	OnFCC	-268091.87	-2424.11	-265667.00	4.51	-508.5
	$DTPi^-$	OnHCP	-268092.15	-2424.11	-265667.00	4.51	-535.5

Table 3. Ligand binding energies for H_2O and OH^- on Sp, $(Ni,Fe)_8S_9$ and Pt, calculated as per Equation 4 for neutral species and Equation 5 for anionic species.

Surface	Ligand	Surface coverage /binding motif	Ligands per unit cell	$[L+S]^0$ (eV)	$[L]^x$ (eV)	$[S]^0$ (eV)	$\phi_{[S]^0}$ (eV)	Total B.E. (kJ mol^{-1})	Binding energy per ligand
Sp	H_2O	1/2	1	-34048.79	-473.04	-33575.53	–	-21.5	–
	H_2O	full	2	-34522.21	-946.08	-33575.53	–	-58.0	-29.0
	OH^-	1/2	1	-134760.67	-456.24	-134304.43	4.91	-473.8	–
	OH·	1/2	1	-134760.67	-453.39	-134304.43	–	-274.1	–
Ni-Pn	H_2O	1/3	1	-23586.40	-473.04	-23113.15	–	-20.4	–
	H_2O	2/3	2	-24060.17	-473.04	-23113.15	–	-90.3	-45.2
	H_2O	full	3	-24533.72	-473.04	-23113.15	–	-139.8	-46.6
	OH^-	1/3	1	-23569.83	-456.24	-23113.15	4.99	-523.9	–
	OH·	1/3	1	-23569.83	-453.39	-23113.15	–	-344.0	–
Fe-Pn	H_2O	1/3	1	-23582.33	-473.04	-23108.58	–	-68.8	–
	H_2O	2/3	2	-24056.04	-473.04	-23108.58	–	-132.6	-66.3
	H_2O	full	3	-24529.72	-473.04	-23108.58	–	-194.9	-65.0
	OH^-	1/3	1	-23566.39	-456.24	-23108.58	4.33	-569.3	–
	OH·	1/3	1	-23566.39	-453.39	-23108.58	–	-425.8	–
Pt	H_2O	on-top	1	-149911.22	-473.04	-149437.85	–	-32.1	–
	H_2O	bridge	1	-149910.95	-473.04	-149437.85	–	-5.6	–
	H_2O	flat ice	6	-152279.08	-2838.24	-149437.85	–	-288.1	-48.0
	H_2O	on-top	1	-149911.22	-473.04	-149437.85	–	-32.1	–
	OH^-	on-top	1	-149894.32	-456.24	-149437.85	5.66	-568.3	–
	OH·	on-top	1	-149894.32	-453.39	-149437.85	–	-297.1	–
	OH^-	bridge	1	-149894.35	-456.24	-149437.85	5.66	-571.2	–
	OH·	bridge	1	-149894.35	-453.39	-149437.85	–	-300.2	–

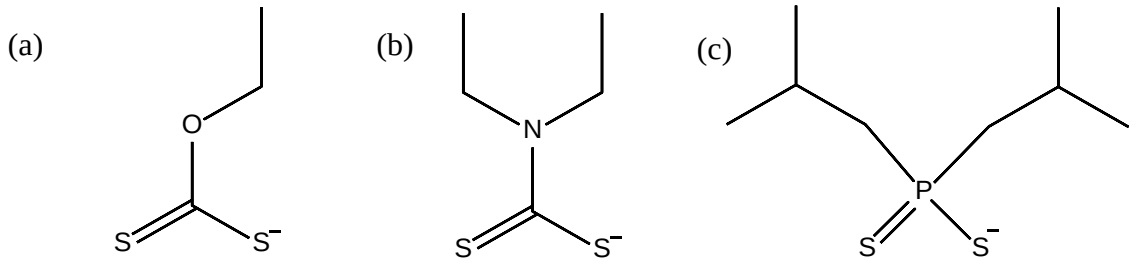

Figure 1: (a) ethyl xanthate (EX), (b) diethyldithiocarbamate (DEDTC) and (c) diisobutyl dithiophosphinate (DTPi).

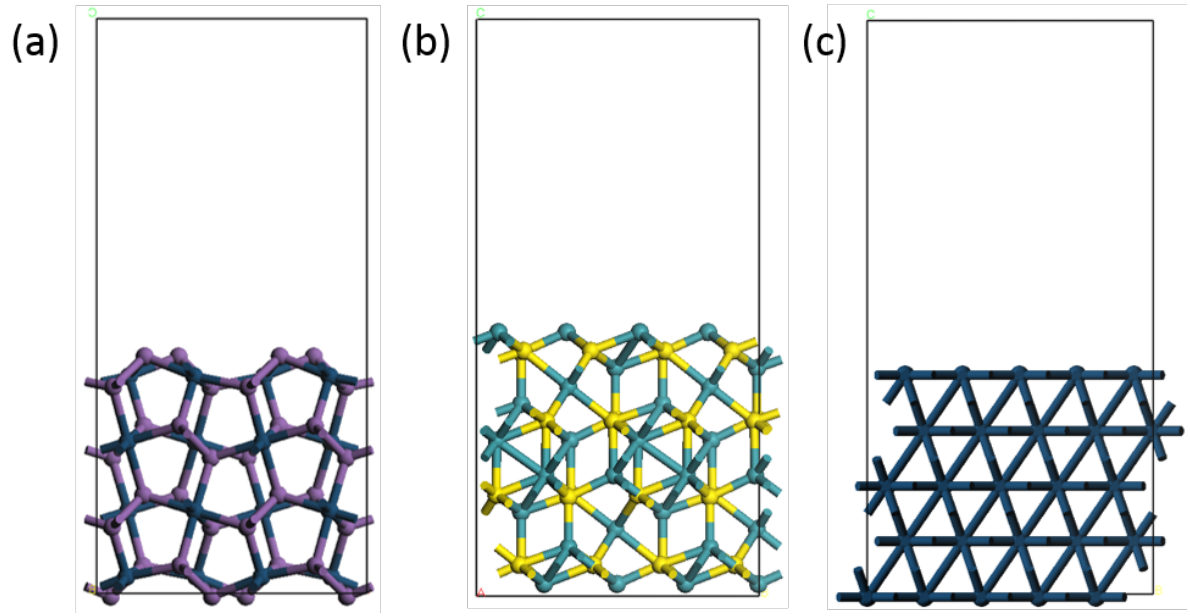

Figure 2: Working surfaces (a) [100] As-terminated Sp, (b) [111] Metal-terminated Pn and (c) [111] Pt.

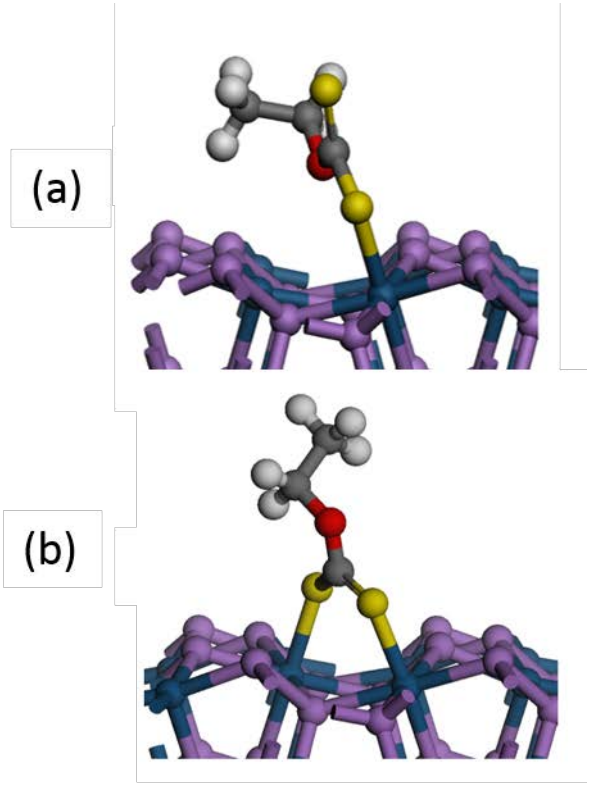

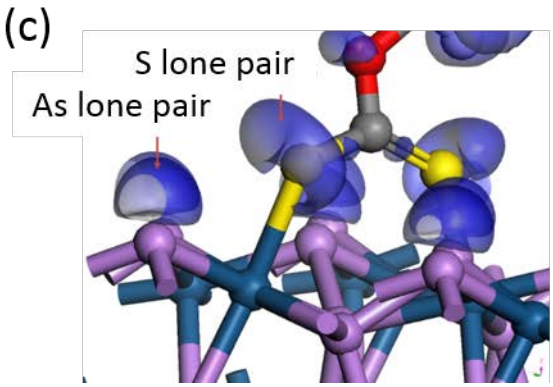

Figure 3. Optimised geometries for (a) monodentate and (b) bridging EX on Sp. Red arrows indicate which surface metal atom is being addressed. (c) ELF plot for bridging EX on Sp. Legend: Purple – As, Blue – Pt, Yellow – S, Grey – C, Red – O, White – H.

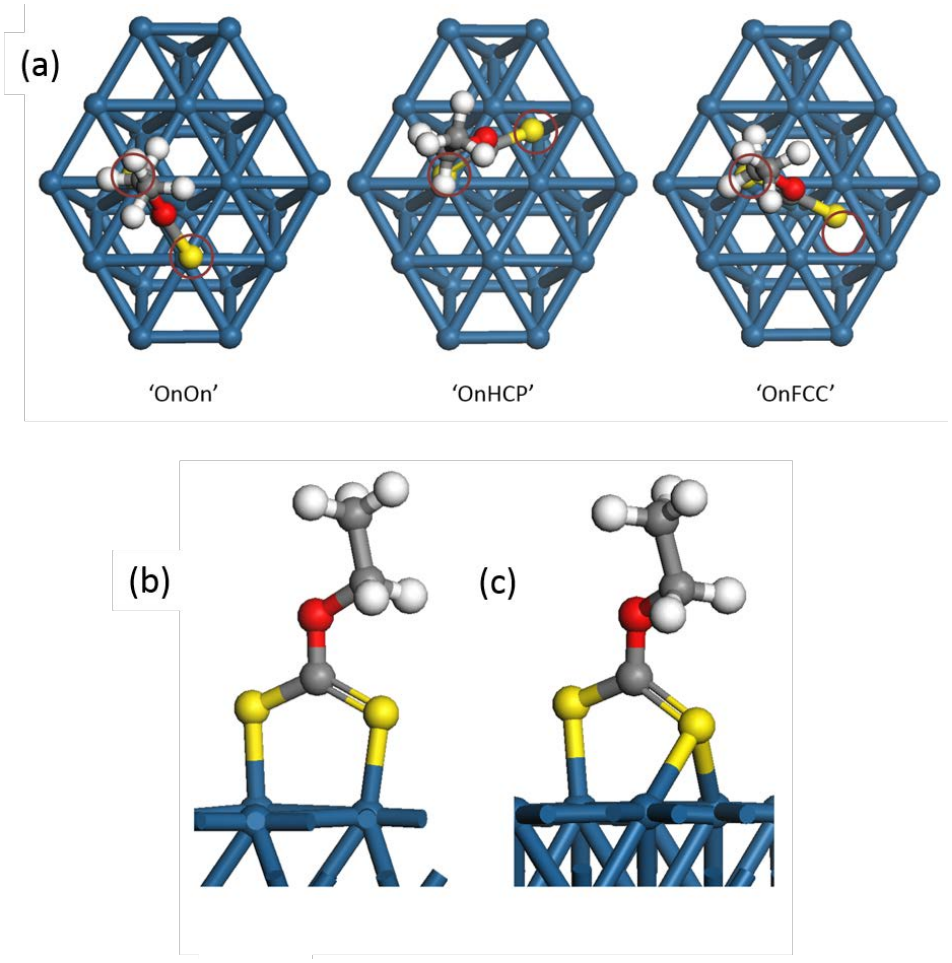

Figure 4. (a) Top-down view of **i**nput structures for the 'OnOn', 'OnHCP' and 'OnFCC' models of EX on the Pt surface, with red circles highlight the Pt surface binding sites being addressed in each case. (b) 'OnOn' and (c) 'OnHCP/OnFCC' optimised structures. Legend: Blue – Pt, Red – O, Yellow – S, Grey – C, White – H.

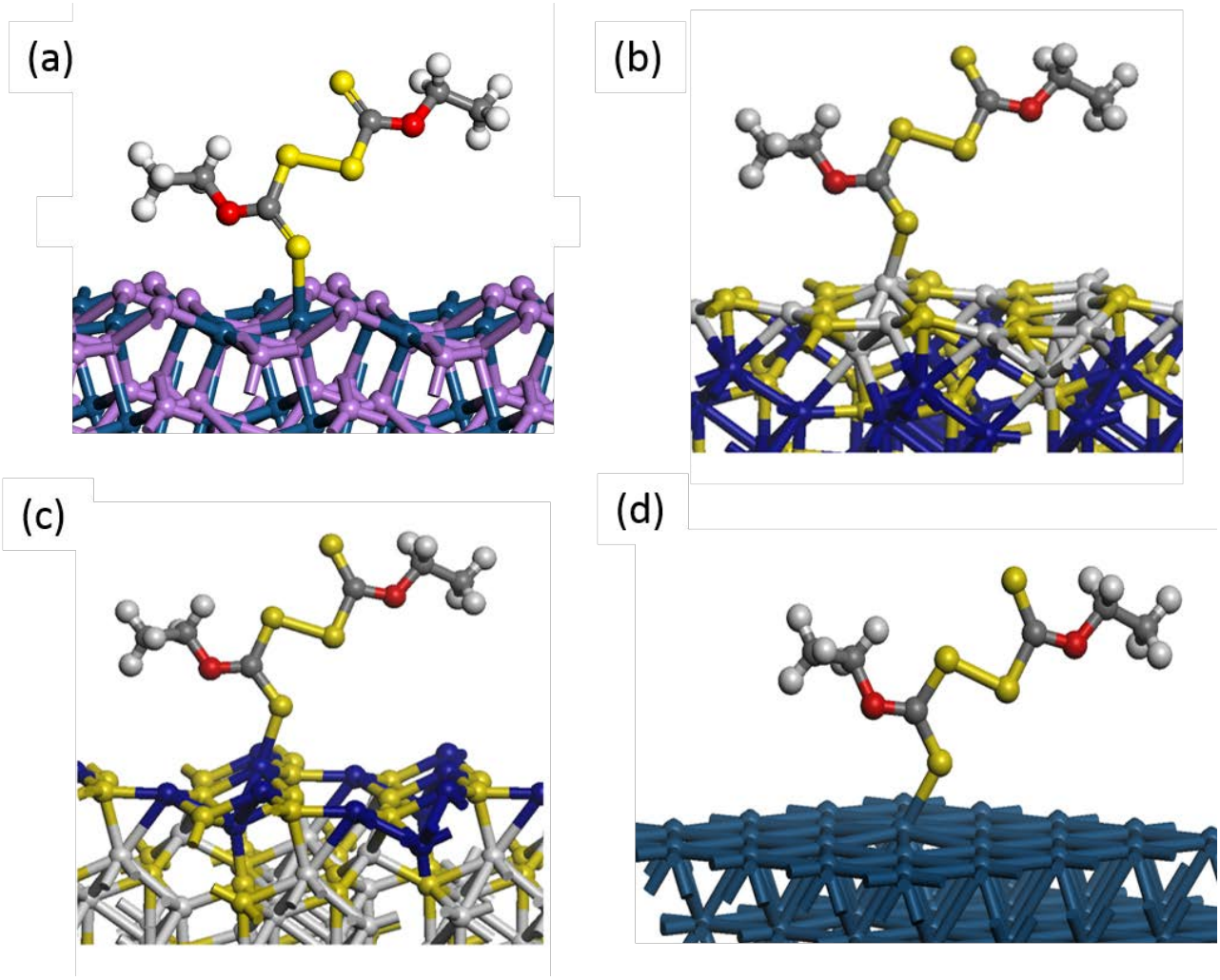

Figure 5. Optimised output geometries for $(EX)_2$ on (a) Sp (b) N-Pn , (c) Fe-Pn and (e) Pt . Legend: Purple – As, Blue – Pt, White (in surface) – Ni, Blue (in surface) – Fe, Yellow – S, Grey – C, White (on ligand)– H.

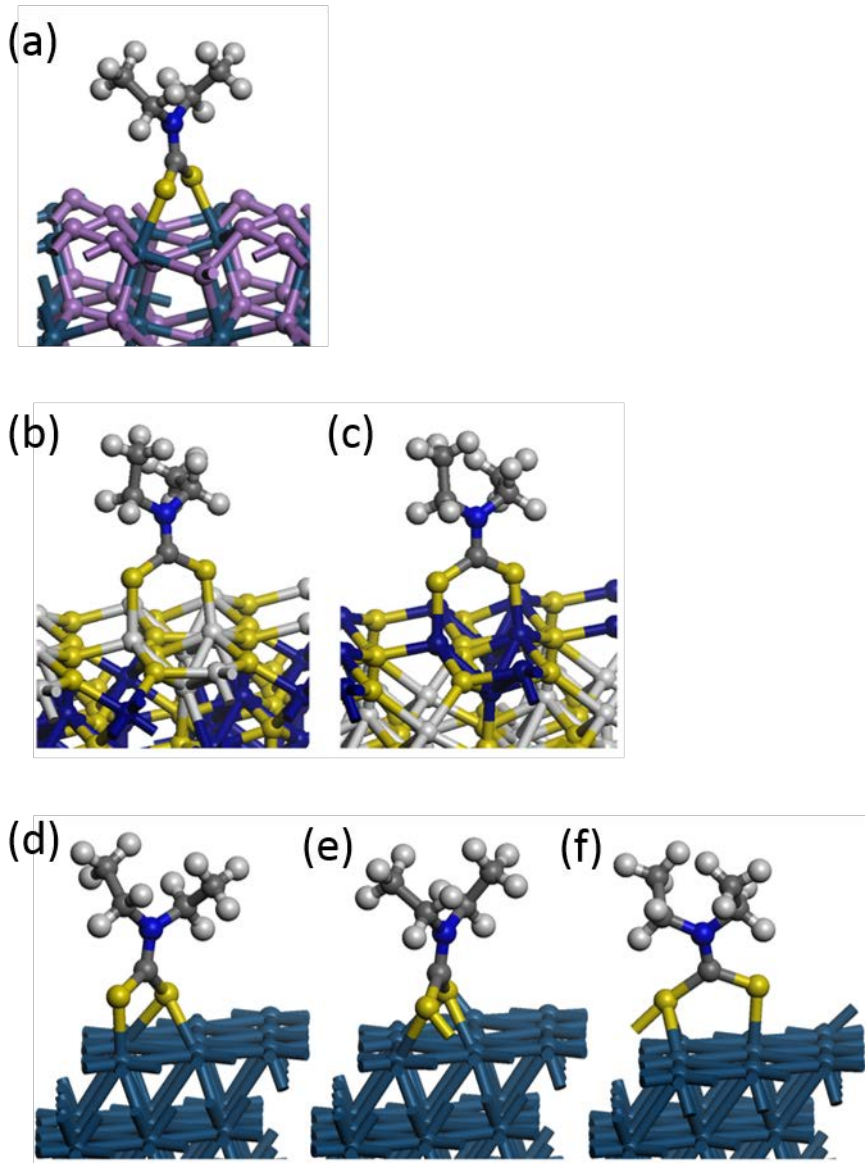

Figure 6. Optimised output geometries for DEDTC on (a) Sp, (b) Ni-Pn, (c) Fe-Pn, (d) Pt (OnOn binding site), (e) Pt (OnFCC bonding site) and (f) Pt (OnHCP binding site). Legend: Purple – As, Blue – Pt, White (in surface) – Ni, Blue (in surface) – Fe, Yellow – S, Grey – C, White (on ligand)– H.

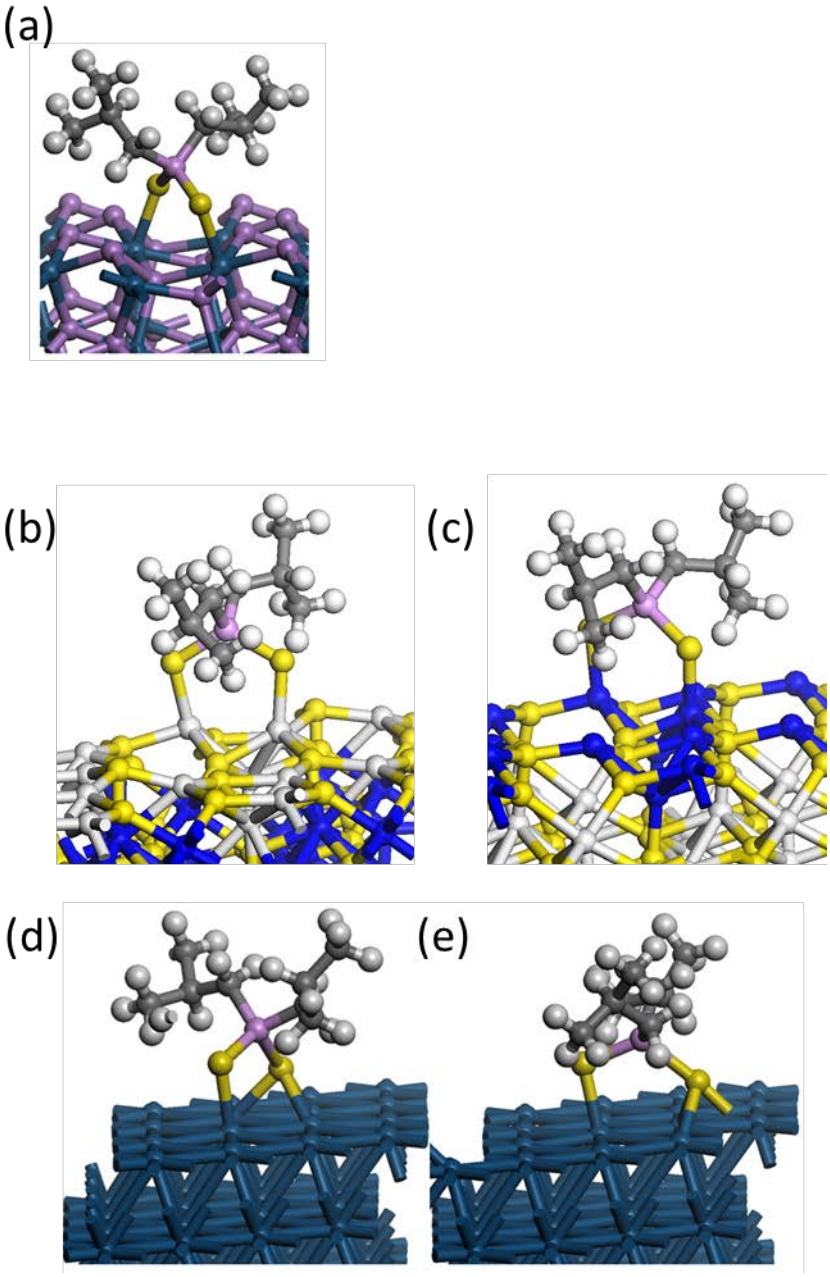

Figure 7. Optimised output geometries for DTPi on (a) Sp, (b) Ni-Pn, (c) Fe-Pn, (d) Pt (OnFCC bonding site) and (e) Pt (OnHCP binding site). Legend: Purple – As, Blue – Pt, White (in surface) – Ni, Blue (in surface) – Fe, Yellow – S, Grey – C, Pink – P, White (on ligand)– H.

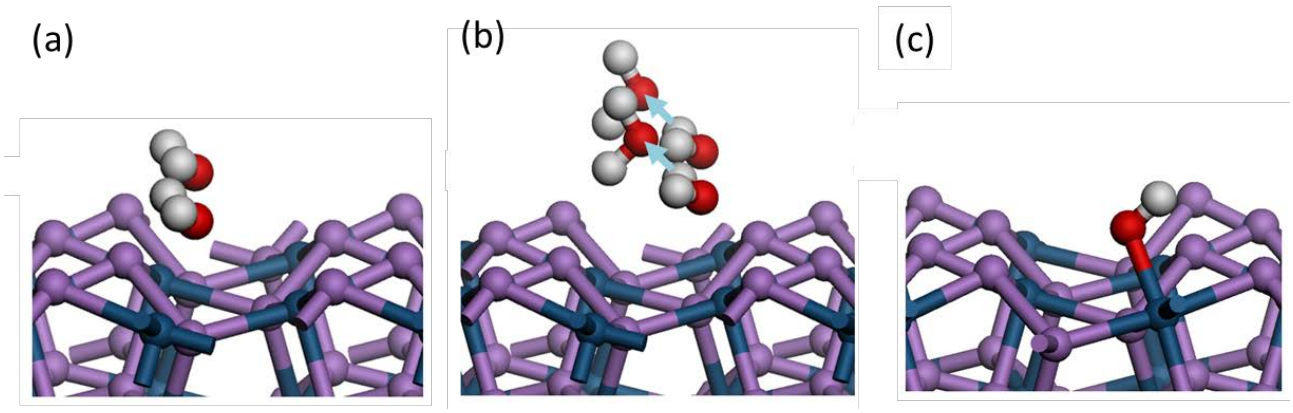

Figure 8. Optimised geometries for (a) half-monolayer H_2O (b) full-monolayer H_2O adsorption and (c) half-monolayer OH^- on Sp. Pale blue arrows indicate hydrogen bonds. Legend: Purple – As, Blue – Pt, Red – O, White – H.

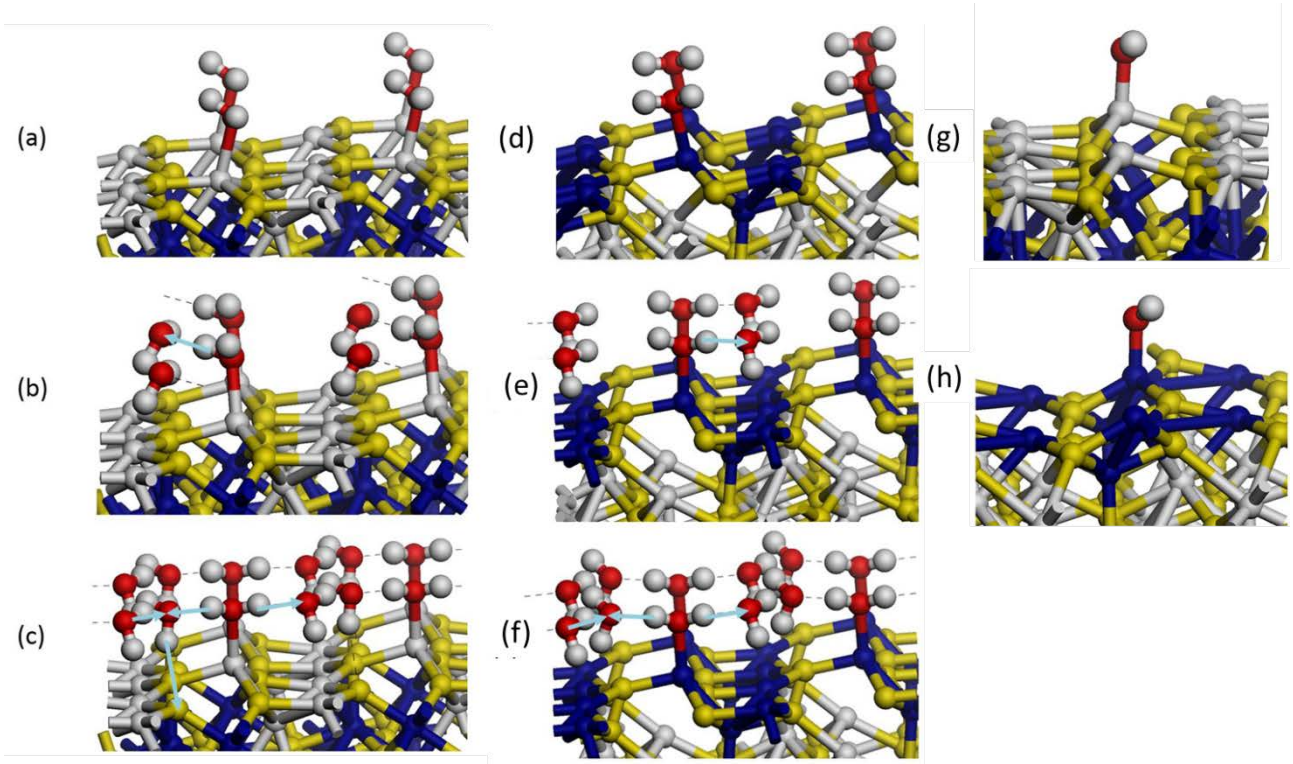

Figure 9. Optimised geometries for 1/3rd (a, d), 2/3rd (b,e) and full surface coverage (c,f) on Ni-Pn and Fe-Pn, respectively, along with single adsorption OH^- Ni-Pn (g) and Fe-Pn (h). Pale blue arrows indicate hydrogen bonds. Legend: White (in surface) – Ni, Blue (in surface) – Fe, Yellow – S, Grey – C, White (on ligand)– H.

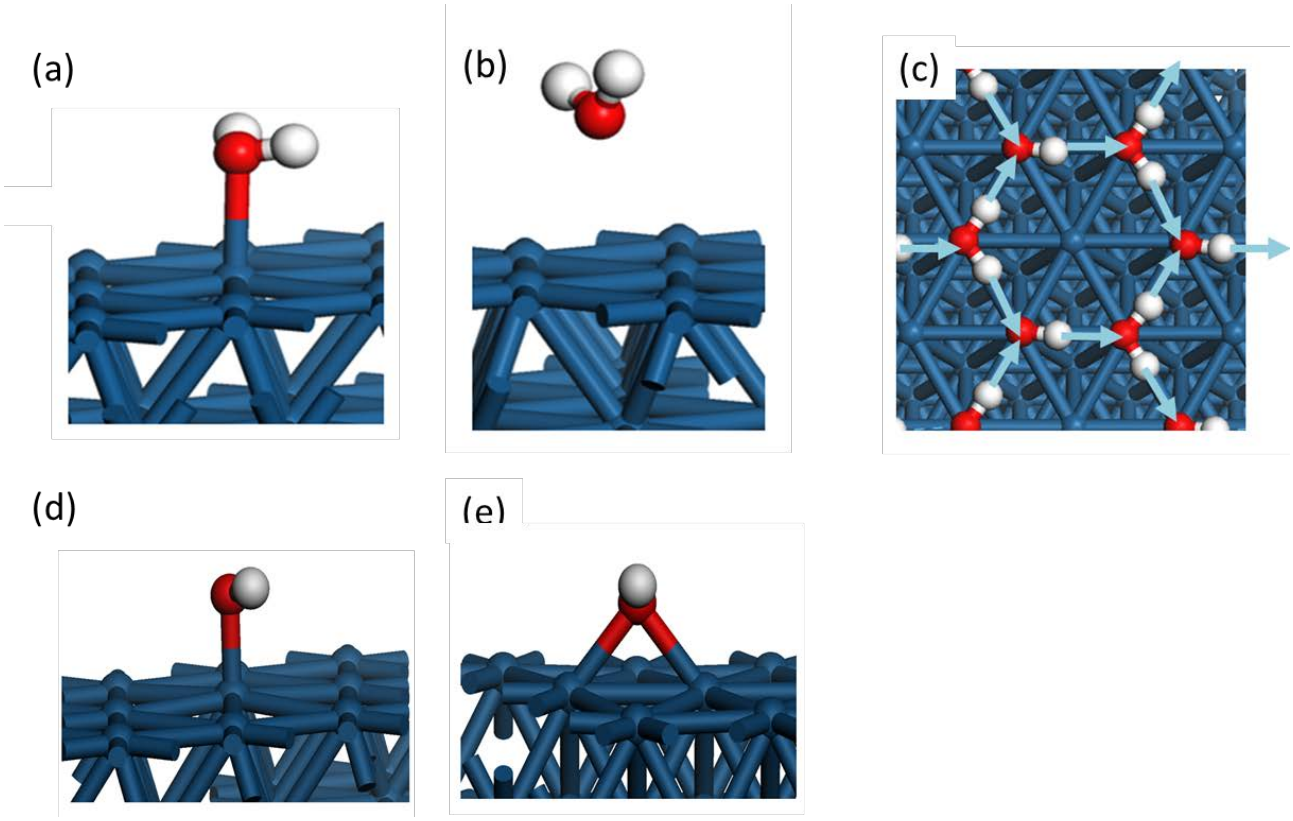

Figure 10. Optimised geometries for (a) on-top H_2O (b) bridge H_2O and (c) full monolayer on Pt, (d) on-top, (e) bridge binding sites for OH^- on Pt. Pale blue arrows indicate hydrogen bonds. Legend: Blue – Pt, Red – O, White – H.

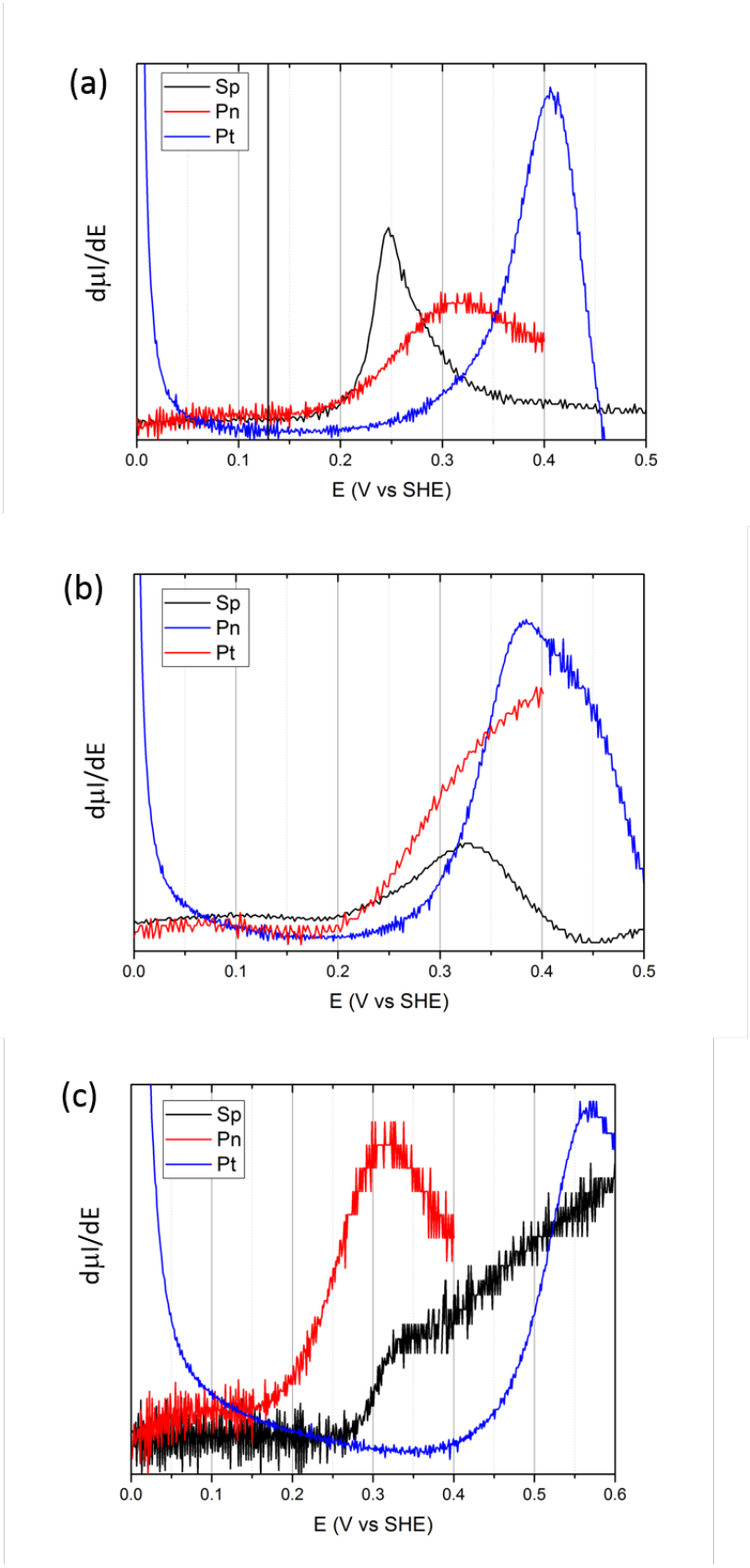

Figure 11 Normalised differentiated anodic currents for (a) EX, (b) DEDTC and (c) DTPi for Sp, Pn and Pt working electrodes. The equilibrium potential for EX/EX_2 at $1x10^{-3}$ M [0.121 V (SHE)] is indicated by the vertical black line in (a).

Table of Contents Graphic